

# Mechanical Modulation of 2D Electronic Devices at Atto-Joule Energy via Flexotronic Effect

Pengwen Guo, Mengmeng Jia, Di Guo, Wei Wang, Yufei Zhang, Lele Ren, Aifang Yu, Zhong Lin Wang,\* and Junyi Zhai\*

In addition to electrical, optical, and magnetic fields, mechanical forces have demonstrated a strong ability to modulate semiconductor devices. With the rapid development of piezotronics and flexotronics, force regulation has been widely used in field-effect transistors (FETs), human–machine interfaces, light-emitting diodes (LEDs), solar cells, etc. Here, a large mechanical modulation of electronic properties by nano-Newton force in semiconductor materials with a large Young's modulus-based force FET is reported. More importantly, this FET has ultralow switching energy dissipation (7 aJ per decade current gain) and nearly zero leakage power; these values are even better than those of electronic FETs. This finding paves the way for practical applications of nanoforce modulation devices at high power efficiency.

nearly all semiconductor materials,<sup>[4–6]</sup> with a linear modulation of the semiconductor properties under an applied force.<sup>[7]</sup> However, the tuning ratio is low for most semiconductor materials. In 2007, the piezotronic effect (PE) was proposed to modulate the electrical properties in piezoelectric semiconductor-based heterostructures (Schottky junctions or p-n junctions) via the piezoelectric effect.<sup>[8,9]</sup> The PE can exponentially tune electronic or optoelectronic properties by changing the bandgap of the heterostructure by means of the piezoelectric potential at the interface under an applied external force, thus dramatically enhancing the sensitivity of

## 1. Introduction

The rapid growth of semiconductor physics has promoted the continuous development of information technology. Most of these works focus on the electrical, optical, and magnetic properties and their coupling effects in semiconductor materials or heterostructures. With the rapid development of electronic devices and the great demand for human–machine interfaces, the coupling effect between force and semiconductor properties has drawn increasing attention, especially in the last 20 years.<sup>[1–3]</sup> The piezoresistive effect can be observed in

piezotronic force sensors or improving semiconductor properties with the applied force.<sup>[10–12]</sup> However, the PE requires semiconductor materials to have piezoelectric properties; thus, in many important semiconductor materials (such as silicon and germanium), this effect cannot be used to improve electrical, phototronic or magnetic properties. Even in piezoelectric<sup>[13]</sup> semiconductors, there is no piezotronic effect along the unpolarized direction.

The coupling between electric polarization and the strain gradient, namely, flexoelectricity,<sup>[14–16]</sup> describes the contribution to the thermodynamics of a solid and widely exists in all dielectric materials in any space group, even centrosymmetric semiconductors.<sup>[17–19]</sup> By these means, mechanical modulation of semiconductor properties can be expanded from piezoelectric semiconductors to all semiconductors, and the flexoelectricity can even enhance piezoelectrical properties,<sup>[20,21]</sup> which has promoted the wide implementation of flexoelectronics<sup>[19]</sup> (simplified as flexotronics). However, as the Young's modulus of an inorganic semiconductor is large,<sup>[22,23]</sup> the force and energy required for each modulation are large, and these are key obstacles to the further development and actual application of the mechanical modulation of electronic or optoelectronic devices. Unlike the piezoelectric effect, the flexoelectric effect shows an attractive thickness dependence.<sup>[24,25]</sup> Under a fixed external force, the flexoelectric response is dramatically enhanced when the thickness is reduced to the nanoscale,<sup>[26–28]</sup> which is attributed to the allowable large strain gradient at nanoscale sizes. Alternatively, to achieve a designated flexoelectric response, decreasing the thickness is an effective method for reducing the externally applied force. Therefore, there should be a large flexoelectric modulation of the electronic and optronic properties in ultrathin semiconductor materials under a very small external force.

P. Guo, M. Jia, D. Guo, W. Wang, Y. Zhang, L. Ren, A. Yu, Z. L. Wang, J. Zhai  
Beijing Institute of Nanoenergy and Nanosystems  
Chinese Academy of Sciences  
Beijing 101400, P. R. China

E-mail: zhong.wang@mse.gatech.edu; jyzhai@binn.cas.cn

P. Guo, M. Jia, W. Wang, Y. Zhang, L. Ren, A. Yu, Z. L. Wang, J. Zhai  
School of Nanoscience and Technology  
University of Chinese Academy of Sciences  
Beijing 100049, P. R. China

D. Guo, A. Yu, J. Zhai

Center on Nanoenergy Research  
School of Physical Science and Technology  
Guangxi University  
Nanning, Guangxi 530004, P. R. China

Z. L. Wang

School of Materials Science and Engineering  
Georgia Institute of Technology  
Atlanta, GA 30332, USA

 The ORCID identification number(s) for the author(s) of this article can be found under <https://doi.org/10.1002/adfm.202202779>.

DOI: 10.1002/adfm.202202779

Field-effect transistors (FETs) are the most important basic electronic devices in information technology. The development of integrated circuits (ICs) requires large-scale integration of FETs to improve performance and energy efficiency and to obey Moore's law.<sup>[29]</sup> However, as the size of the classic Si FET approaches the quantum limit,<sup>[30]</sup> designing a new principle for FETs becomes increasingly important. The main energy consumption of a FET involves two aspects: one is the energy for switching the "on" and "off" states of the FET and the other is the electrical energy leakage from the gate to the source and drain when the FET is in the "on" status.<sup>[31]</sup> A mechanical FET does not have an electrical gate, which means that there is no energy consumption when the FET is in the "on" state.<sup>[32]</sup> When the semiconductor is thin enough, the energy for switching the "on" and "off" states of a mechanical FET can be even lower than the electrical switching energy in typical FETs.

In this work, we report the mechanical modulation of electronic properties by nano-Newton forces in single-layer MoS<sub>2</sub>-based devices. Here, MoS<sub>2</sub> is just a representative material, and any ultrathin semiconductor material can be substituted. Our mechanical modulation of electronic devices (MMEDs) based on a single-layer MoS<sub>2</sub> suspension structure can achieve significant transport modulation with a strain gauge factor (GF) of up to 4801 by the flexotronic effect (FE), far outperforming conventional piezoelectric, piezoresistive, and capacitive electronics;<sup>[33]</sup> moreover, the switching energy dissipation is extremely reduced, to the attojoule level (7 aJ per decade current gain), by the nano-Newton tip-force, and the leakage power approaches zero if other mechanical losses are excluded, which can decrease the energy consumption of the electronics in the design principle. This work demonstrates that electronic devices can be effectively modulated by ultrasmall forces through the FE and offers a new means to compensate for low heat generation and extremely low power consumption ICs.

## 2. Results and Discussion

### 2.1. Fabrication and Characterization of MMEDs

The FE was explored during the nanoindentation process. This approach can not only achieve a high strain gradient ( $\approx 1.3 \times 10^5 \text{ m}^{-1}$ ) by utilizing nonlinear bending deformation but also effectively distinguish the relative contributions of flexoelectricity and piezoelectricity to the resulting polarization.<sup>[34]</sup> MoS<sub>2</sub> flakes were exfoliated by micromechanical cleavage, and the number of layers was confirmed to range from single layers to trilayers based on the differences between the peak positions of the E<sub>2g</sub><sup>1</sup> and A<sub>1g</sub> modes in the Raman spectra (Figure 1d) and the height profiles of atomic force microscope (AFM) scan images. The selected MoS<sub>2</sub> thin films were transferred onto a perforated indium tin oxide (ITO)/glass substrate. Then, the morphologies and flexotronic properties of the films were studied by conductive AFM (C-AFM) mode, in which high-conductivity, high-transparency, and simple-etching ITO were used as the bottom electrode, as shown in Figure 1a. The polarization potential induced by the FE can be regarded as a "gate" modulating the electronic process, as shown in the equivalent circuit diagram in the middle. In situ measurements of the

nanoindentation test and electrical transport could be implemented synchronously by a C-AFM probe. Here, the probe had a radius of 30 nm (Figure 1b) to ensure nonlinear bending behavior for ultrathin films under nanoindentation testing. An optical photograph (Figure 1c) of the array of circular wells (diameters  $\approx 2 \mu\text{m}$ , depth  $\approx 260 \text{ nm}$ ) and one MoS<sub>2</sub> flake spanning over the wells is presented. A tapping mode AFM image (Figure S1a, Supporting Information) indicates the suspension structure of the MoS<sub>2</sub> film, and the inset reveals that the film adheres to the sidewall of the well at a depth of  $\approx 10 \text{ nm}$ . The adhesion may be due to van der Waals interactions and contraction effects during the process of the dry-transfer technique, which is the probable origin of the film pretension.

For a Schottky contact device, the area of the interface in the metal-semiconductor contact may affect electrical transport when the external circuit is at a fixed voltage bias. To evaluate the concrete contribution of the contact resistance (CR) of the AFM probe and the MoS<sub>2</sub> film to electrical transport during the nanoindentation test, we designed a CR device; the schematic diagram is shown in Figure 1e, where one half of the single-layer MoS<sub>2</sub> was mechanically deposited on an ITO substrate with a 10-nm HfO<sub>2</sub> epilayer (shown in Figure 1g, with the inset AFM height profile along the white dotted line). Figure 1f shows the optical image of the device, illustrating the actual structure of our device by color contrast, and Figure 1g shows a scanning electron microscope (SEM) image of the device, indicating that the single-layer MoS<sub>2</sub> tightly contacts both the HfO<sub>2</sub> and ITO substrates without visible wrinkles or discontinuities, which ensures the accuracy and effectiveness of the subsequent nanoindentation test. The yellow and blue dashed lines display the test region for 1 and 2 L flakes, which ensures that the carrier transport channel length is the same as that of the corresponding layers of the suspension device for comparison with their current levels (SEM images of the suspension structure are shown in Figure S1b, Supporting Information).

To verify the FE in an ultrathin electronic device, we first measured the electrical transport of a typical single Schottky junction modulated by a flexoelectric polarization field induced by a strain gradient under a voltage bias in the suspension structure MMEDs (Figure 2a). The forward current increases steadily with increasing load, whereas the reverse current remains comparable to the noise level below 200 nN. The later increase may be due to the existence of a barrier between the flake and the substrate ( $\phi_{\text{fs}}$  in Figure 3c), which is certainly due to the FE. Our single-layer MMEDs display a minimum force response (1 nN) during the measurement test when withstanding a load in the range of 1–7 nN, which illustrates a fascinating force/strain-gradient resolution of the FE in 2D materials.

The film is presumed to deform smoothly under the indenter as long as the AFM tip is recognized as an ideal hemisphere. During the nanoindentation test, the contact area between the AFM conductive probe and the MoS<sub>2</sub> flake increases, which leads to the expansion of the Schottky junction area and further influences the transport of the majority carriers. We characterized the electrical transport properties of the contact resistant device under AFM tip nanoindentations, and the current–voltage (*I*–*V*) characteristics change with increasing force (Figure 2b). This variation may be due to the interstices

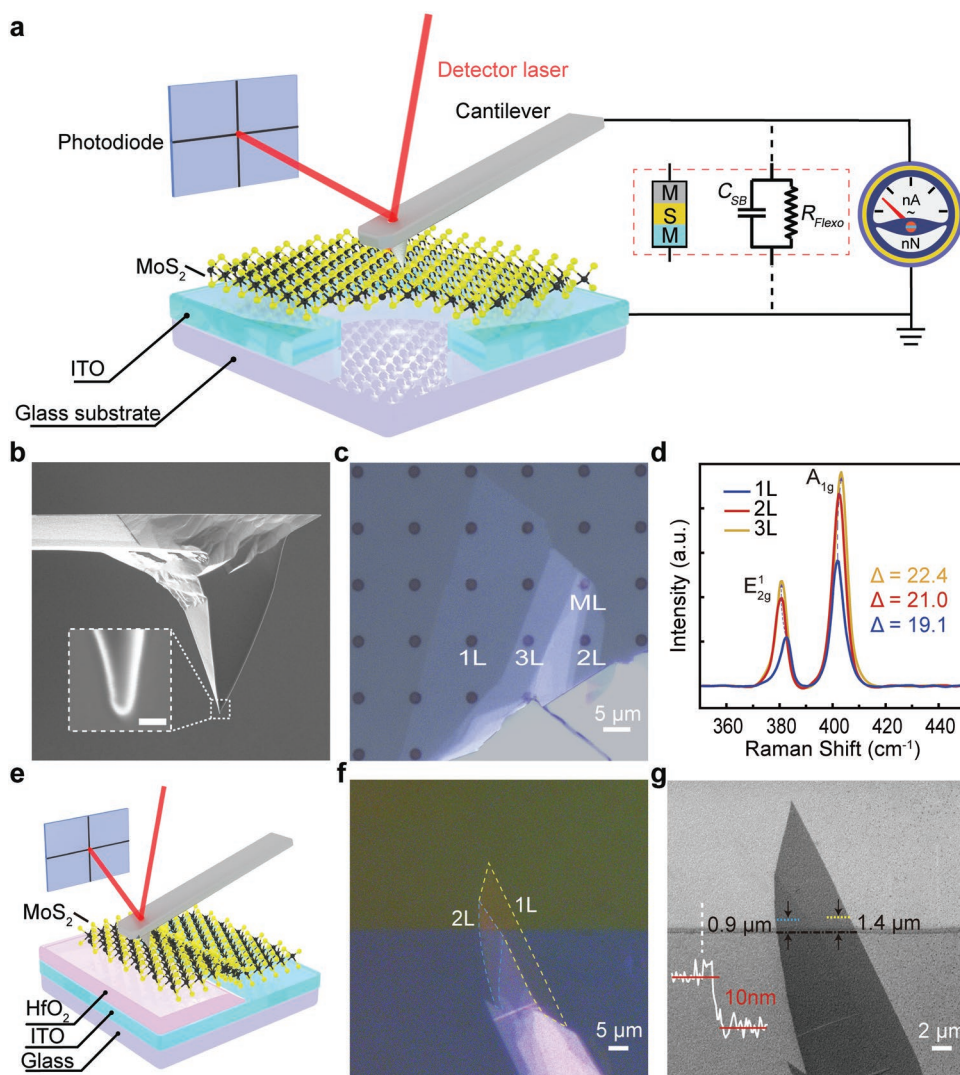


**Figure 1.** Fabrication and characterization of the MMEDs. a) Three-dimensional schematic of the MMEDs and its equivalent circuit diagram. The region delineated by red dashed lines is a two-terminal device, in which  $R_{\text{Flexo}}$  represents the equivalent tunable resistor modulated by a strain gradient and light, and  $C_{\text{SB}}$  represents the equivalent parallel capacitance. b) The SEM images of probe-tip topography before nanoindentation test. Scale bar, 100 nm. c) The optical microscopy image, d) Raman spectra (excited by 532 nm laser) of 1, 2, and 3 L MoS<sub>2</sub> flakes. e) Three-dimensional schematic of the designed MoS<sub>2</sub> contact resistance device. f) The optical microscopy image, g) SEM image of the MoS<sub>2</sub> flake upon the patterned HfO<sub>2</sub>/ITO substrate (inset shows the thickness of the HfO<sub>2</sub> layer; yellow and blue dashed lines display the region of test for 1 and 2 L flakes, respectively).

existing between the flake and HfO<sub>2</sub> substrate, leading to a small increment and then a stable current, with tight contact occurring. Moreover, to further explore the effect of the CR, we adopted another conductive Ag-probe ( $W = 4.23$  eV) (ref. [35]) with a work function smaller than that of the previous Pt-probe ( $W = 5.7$  eV, whereas  $\phi_{\text{B}} = 1.7$  eV) (ref. [36]) to fabricate a device with a lower Schottky barrier height ( $\phi_{\text{B}} < 0.5$  eV) device. Then, we characterized the electrical transport properties of the device under AFM Ag-probe nanoindentations. Figure 2c shows that the  $I$ - $V$  characteristics exhibit typical ohmic contact behavior, and the forward currents are efficiently modulated by the loading force. Then, the current reaches saturation, which indicates the existence of a lower Schottky barrier and can even be considered to represent an ohmic contact device. Depending on the loading force, the rectification ratios of the Schottky/ohmic

contacts reach 45.7 to 2.7 at 1 to 400 nN under a +1 V voltage bias, respectively (Figure S2, Supporting Information). The above measurements indicate that the contribution of CR to carrier transport is appreciably lower than that of the FE.

In addition to the FE and CR, flexoresistive effect (FR) and PE factors may influence the modulation of the loop current if the system's internal resistance and measurement error are neglected. The strain gradient may strongly disturb the band structure of MoS<sub>2</sub> and then affect the bandgap width and the carrier effective masses, leading to the FR, analogous to the piezoresistive effect, and a reduction in the band gap at a rate of  $\approx 59$  meV per percent strain<sup>[37]</sup> for a single-layer MoS<sub>2</sub>. For our MMEDs, the change in Schottky barrier height (SBH) ( $\Delta\phi_{\text{B}}$ ) for a +1 V bias induced by two factors (FE and FR) is shown in Figure 2d, which indicates that the modulation of the barrier

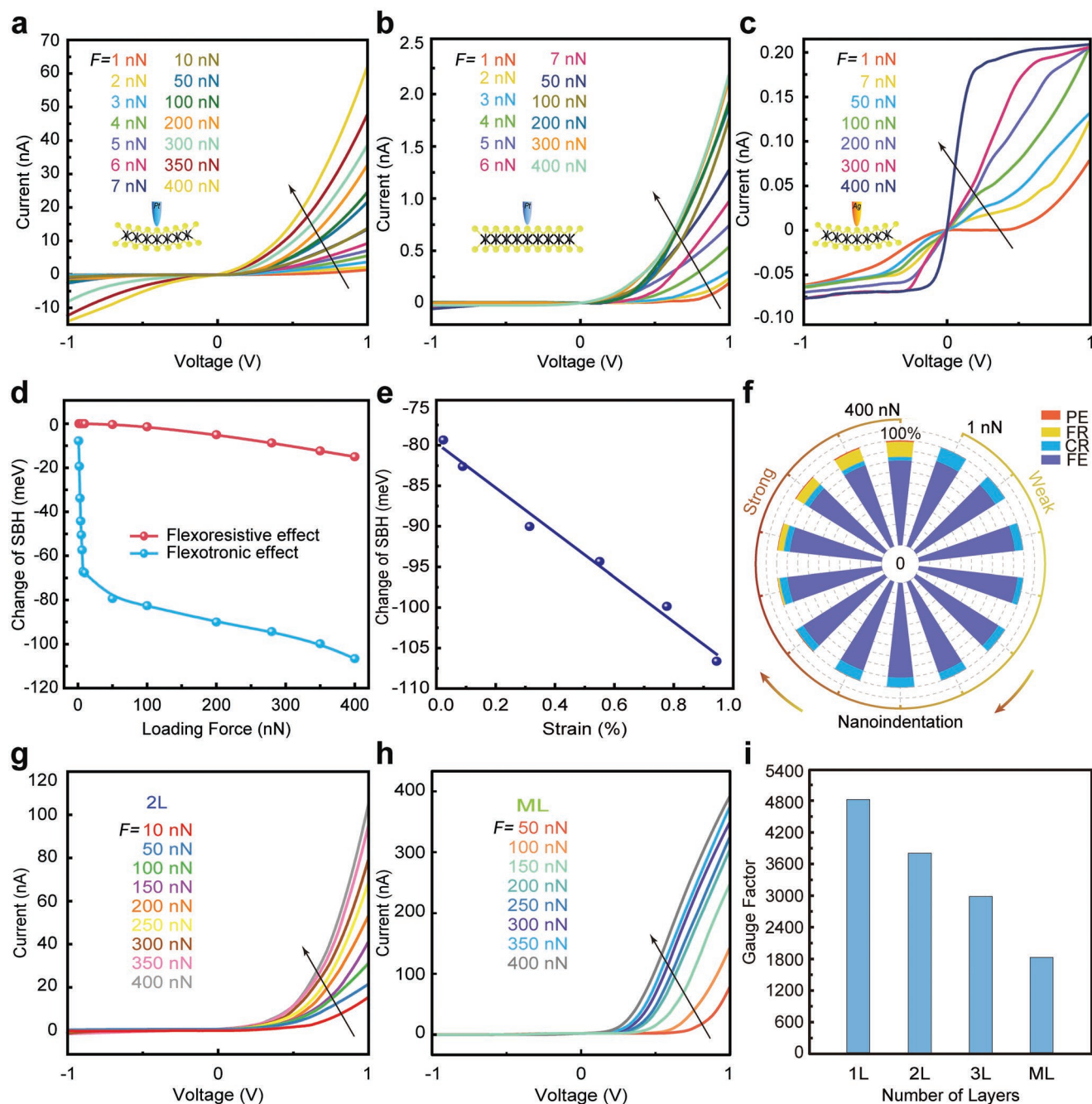


**Figure 2.** The FE in 2D MoS<sub>2</sub> MMEDs. Electrical transport properties of various structure single-layer devices under AFM probe-tip nanoindentation, in which a) suspension structure under Pt-probe, b) contact structure under Pt-probe, and c) suspension structure under Ag-probe, respectively. The derived change in SBH as a function of the loading force d) and strain e) at a bias voltage of +1 V. f) The normalized percent contribution of four factors (PE, FR, CR, and FE) to current modulation at +1 V voltage bias, respectively. Electrical transport properties of suspension structure under Pt-probe for 2 L g) and multilayer/bulk h) MoS<sub>2</sub> flakes; i) The gauge factor of flexotronics in 1, 2, 3 L, and ML MoS<sub>2</sub> MMEDs under the same measuring conditions (the tip-force within 400 nN).

dominates the current transport process. Utilizing the models in Figure S3 (Supporting Information), we can calculate the change in SBH induced by FE/PE, and Figure 2e shows that the change in SBH has an approximately linear relationship with axial strain corresponding to the larger loading force. The inflexion appears because of inhomogeneous strain during nonlinear bending deformation (Figure 2d), which is one factor that differs from the

PE. In addition, we measured the FE in bilayer and bulk MoS<sub>2</sub> (as shown in Figure 2g,h, respectively), which is another factor different from the PE because the piezotronic response exhibits only an odd number of atomic layers MoS<sub>2</sub> in the in-plane direction.<sup>[38]</sup> To intuitively estimate the four effects (FE, CR, FR, and PE) on the modulation of current transport during the nanoindentation test, based on the modulation of the FE, Figure 2f was

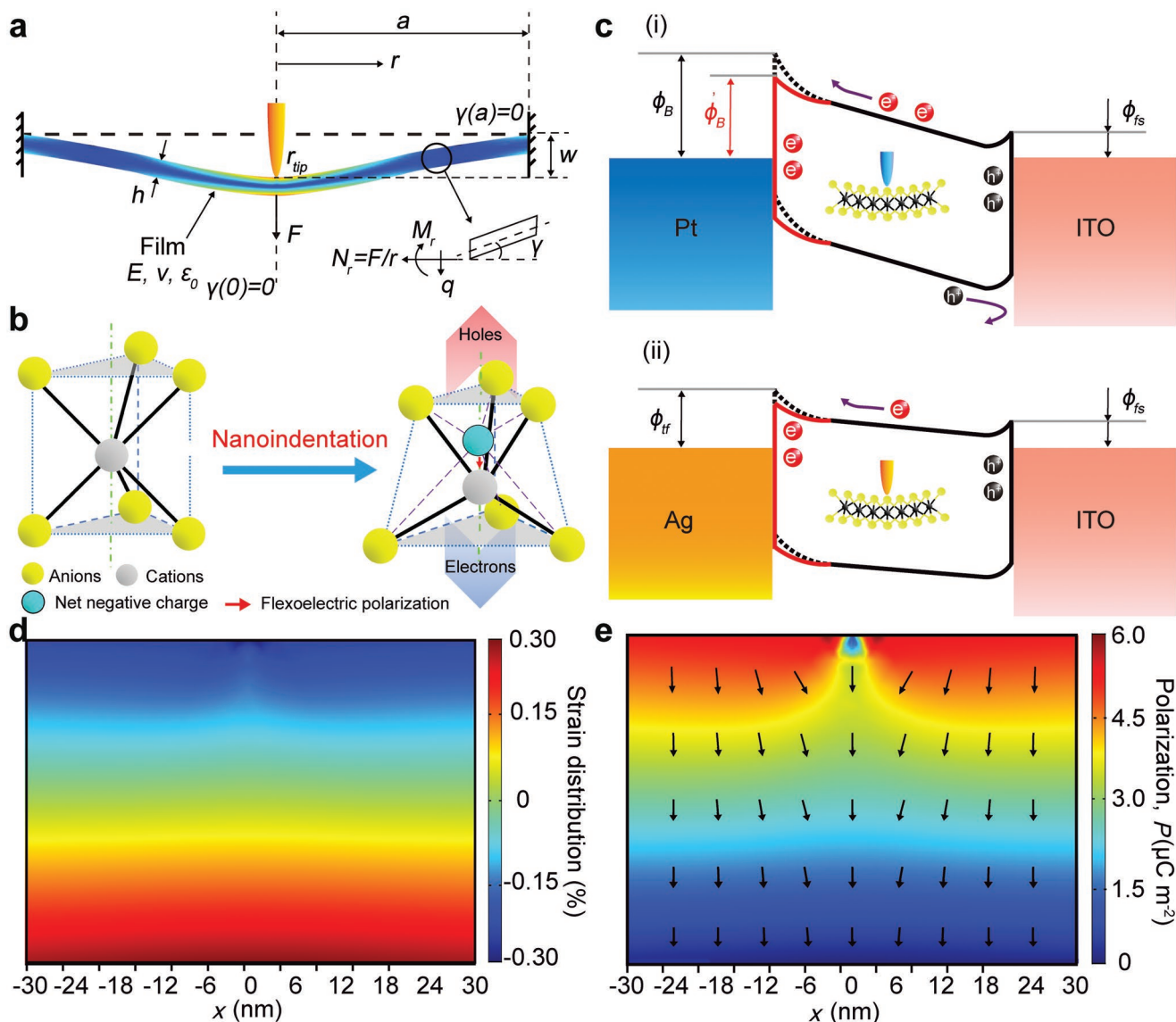


**Figure 3.** The mechanism of flexotronics in 2D MoS<sub>2</sub>. a) Schematic diagram of nonlinear deformation. A circular suspended film with Young's modulus  $E$ , Poisson ratio  $\nu$ , and prestrain  $\varepsilon_0$  is elastically deformed in the middle by an AFM tip. The film is fixed at the edges and is loaded in the center, resulting in a vertical deflection  $w$ . b) Inhomogeneous strained centrosymmetric crystal structure. c) Band diagrams of flexotronic response in the MoS<sub>2</sub> MMEDs. i) the flexotronic behavior induced by strain gradient; ii) the low Schottky contact of the interface between Ag-probe and the film. The symbols “h<sup>+</sup>” (in black) and “e<sup>-</sup>” (in red) represent the strain-induced positive and negative polarization charges.  $\phi_{SB}$  and  $\phi'_{SB}$  represent the Schottky barrier heights formed between metal and semiconductor contacts without and with strain gradient, respectively. The FE in 2D MoS<sub>2</sub> obtained from theoretical simulations with a tip-force model, showing d) the corresponding strain distribution and e) the flexoelectric polarization distribution under a tip-force of 400 nN. Arrows in (e) denote the polarization direction. The force is directed downward by the AFM tip (radius, 30 nm), which is centered at the origin.

plotted to illustrate the force dependence of the normalized percent contribution in the single-layer MoS<sub>2</sub> device under a +1 V voltage bias, which reveals that the FE dominates the modulation of the carrier transport. Moreover, the effect of CR continues throughout the nanoindentation process, which is attributed to the increase in the contact area between the nanoindenter and the film with mechanical deformation. During the strong nanoindentation test, the influence of the FR and the PE on the current modulation appears and increases gradually, but it is much weaker than that of the FE, which illustrates the necessity of small mechanical deformation. Thus, we realize flexotronic

properties in all 2D MoS<sub>2</sub> within this limited test range, and a MMED GF of >4801 is reached (Figure 2i), which is orders of magnitude larger than that of conventional piezoelectric/piezoresistive/capacitive sensors (Table S1, Supporting Information), illustrating the high strain sensitivity of the suspension structure. A stability test (Figure S4a, Supporting Information) shows that the MoS<sub>2</sub> flakes on the perforated substrate do not slip during the nanoindentation test. In addition, the C-AFM measurements proceed synchronously under the nanoindentation test in situ well without visible wrinkles or discontinuities. These results indicate that the elastic deformation of MoS<sub>2</sub> films

under nanoindentation and the loading history cannot affect IV measurements and that the electrical transport of our MMEDs as active electronics depends only on the bias voltage and the present mechanical loading.

## 2.2. Mechanism of the MMEDs

Considering the circular symmetry of the measured structure and the six equivalent crystalline directions (Figure S5, Supporting Information) in the stress–strain response in MoS<sub>2</sub>, an isotropic film is described by Young's modulus  $E$ , Poisson ratio  $\nu$ , and thickness  $h$  (Figure 3a) under nonlinear bending (Figure S6, Supporting Information). Uniaxial point loading, applied by an AFM tip, can generate inhomogeneous strain at the interface of the tip–film contact and localized breaking of the original centrosymmetry, which generates polarization from the net negative charge to the cations after lattice deformation, and the polarization field inside the crystal has an enormous influence on the concentration and distribution of free carriers in the metal–semiconductor (M–S) interface and semiconductor (Figure 3b), which leads to engineering of the M–S interface and the band structure of the semiconductor (as shown in Figure 3c). While MoS<sub>2</sub> is a centrosymmetric semiconductor along the thickness direction, the polarization distributions in the out-of-plane direction are analogous for a single layer and multilayers; hence, a single layer can represent all flakes. For our tip–film model, the strain/polarization distribution within the range of tip radii sufficiently establishes interface engineering; the local strain distribution in MoS<sub>2</sub> calculated from the  $x$  and  $z$  components is shown in Figure 3d, and Figure 3e shows the simulated flexoelectric polarization distribution under the same mechanical deformation (the related simulation distributions from side views of the whole film are shown in Figure S7, Supporting Information). In fact, we referenced related reports<sup>[39–41]</sup> about the electromechanical response of 2D semiconductors and found that there seem to be no previous direct measurements of flexoelectric polarization; most flexoelectric polarization was calculated by the strain/strain gradient. In our measurements, the maximum out-of-plane polarization  $P$  is  $\approx 5.7 \mu\text{C m}^{-2}$  below the center of the contact area (the force-dependent polarization induced by FE/PE is shown in Figure S8, Supporting Information), which is the same magnitude as the theoretical values ( $\approx 1.5 \mu\text{C m}^{-2}$ ) (ref. [34]).

For our MMEDs, the change in SBH ( $\Delta\phi_{\text{B}}$ ) induced by FE under uniaxial point loading ( $F$ ) can be calculated by (Supporting Information Text).

$$\Delta\phi_{\text{B}} = -\frac{8\pi\mu_{\text{mn}}f(\nu)E^{1/3}a^{-2/3}qw_{\text{d}}(Fh)^{1/3}}{(Ea)^{2/3}\kappa_0h^{2/3} + [f(\nu)]^2\kappa_0F^{2/3}} \quad (1)$$

where  $\mu_{\text{mn}}$  is the flexoelectric coefficient,  $f(\nu)$  is a coefficient related to  $\nu$ ,  $a$  is the radii of the wells,  $q$  is the electronic charge,  $w_{\text{d}}$  is the width of the depletion layer, and  $\kappa_0$  is the dielectric constant of MoS<sub>2</sub>. For MoS<sub>2</sub> MMEDs with identical suspension structures, the relationship between  $\Delta\phi_{\text{B}}$  induced by the FE and the thickness of films is  $\Delta\phi_{\text{B}} \approx -h^{-1/3}$  when the loading force is fixed and the change in mechanical properties (such as  $\mu_{\text{mn}}$ ,  $\nu$ , and  $E$ ) for MoS<sub>2</sub> films with different layers is neglected; the

change in SBH versus normalized thickness at 100 nN loading force shows a significantly negative correlation (Figure S9a, Supporting Information), which explains the thickness dependence property of the FE and the excellent performance for our single-layer MoS<sub>2</sub> MMEDs. Conversely, the relationship between the change in SBH and the loading force is  $\Delta\phi_{\text{B}} \approx -F^{1/3}/(0.2681 + F^{2/3})$  under the same prerequisites, which exhibits an apparent positive correlation (Figure S9b, Supporting Information), and the loading force-dependent curve has a large slope under a small load, which reveals why our MMEDs have both nano-Newton resolution and extremely high GF value sensitivity. Furthermore, the switching energy dissipation of the MMEDs is incredibly reduced, to the attojoule level, due to the electromechanical properties of the single-layer MoS<sub>2</sub>.

## 2.3. Power Consumption of the MMEDs

The total power of semiconductor chips includes dynamic power consumption and static power. Dynamic power refers to the power consumed in a complementary metal-oxide-semiconductor (CMOS) circuit when the inputs switch from one level to another and includes both short circuit power and switching power. A Schottky barrier junction-based MMED is analogous to a switching capacitive node, and only the switching power dissipation should be considered for dynamic power. For our MMEDs, the energy consumption per current gain ( $I/I_0$ ), generated by the process of applying force modulation, is defined as the switching energy dissipation, and is equivalent to the mechanical work during the nanoindentation test without considering mechanical and circuit losses. This work can be expressed as  $W = \int Fdw$ , where  $F$  is the applied force of the probe tip, and  $w$  is the deformation of the film. Then, we calculated the current gain and the switching energy dissipation for different layers of MMEDs and plotted their relationship, as shown in Figure 4a, which shows that the switching energy of the single-layer device consumption is mainly located in the attojoule region. Indeed, there exists one subattojoule point ( $\approx 0.67$  aJ) that can realize a definitive current gain, and the switching energy of multilayer device consumption approaches the femtojoule region, which indicates that the 2D MMEDs have ultralow energy dissipation. Referring to the definition of subthreshold swing (SS), we compared the switching energy dissipation per decuple current gain of the MMEDs with other types of devices, and the results are plotted in Figure 4c (refer to Table S4, Supporting Information). Based on the modulation of the carrier realized by the gate potential, we chose three main types of devices: (i) capacitors, such as MOM and MIM; (ii) FETs, such as MOSFET and FinFET; and (iii) junctions, such as MTJ, FTJ, vdWH, and SBJ. Our results show that via the FE, the single-layer MoS<sub>2</sub> MMEDs can implement a decuple current gain that consumes only 7 aJ, showing that the perspective of ultralow power consumption micro/nanodevices are possible; in addition, our MMEDs realize a 1.6 MHz (quality factor  $Q = 404$ ) response for the mechanical switch (Figure 4b), which approaches the read/write speed of a typical mechanical hard drive ( $\text{Mb s}^{-1}$ ), and the switching frequency can be enhanced by changing the tension and well diameter.<sup>[42]</sup>

Static power, namely, leakage power, is consumed by leakage currents even though the electronics are inactive. CMOS

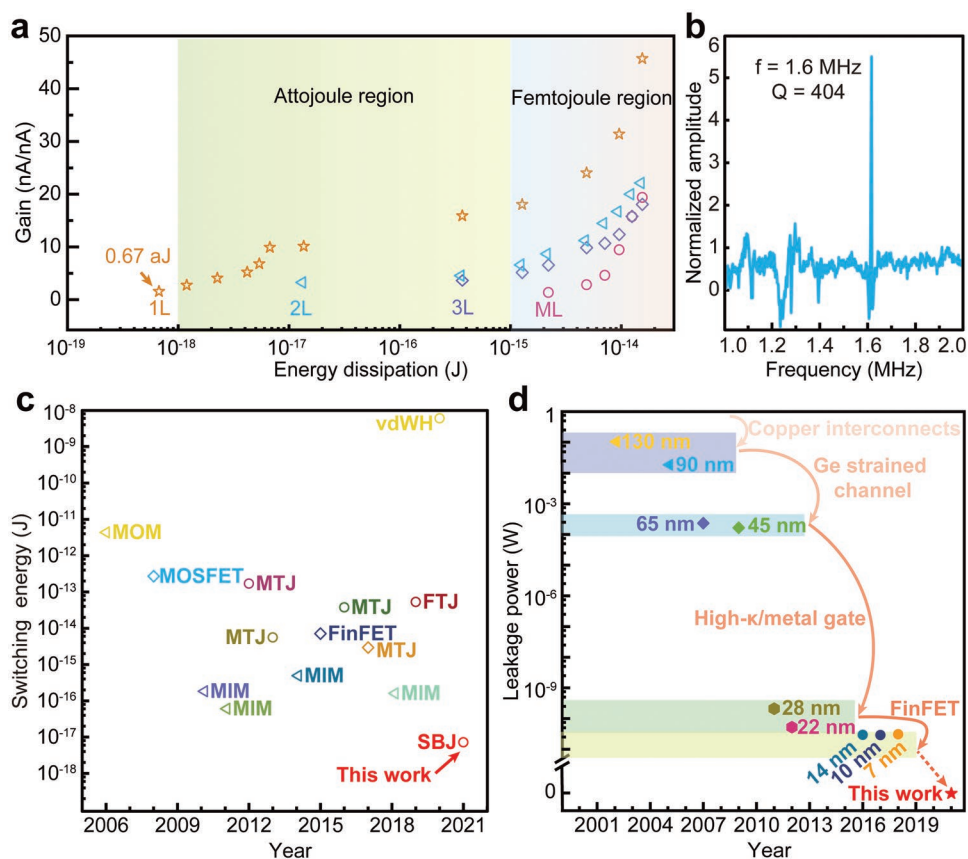


**Figure 4.** Ultralow power 2D MoS<sub>2</sub> MMEDs. a) The switching energy dissipation under different current gain for 1, 2, 3 L, and multilayer MoS<sub>2</sub> devices, respectively. b) The resonance frequency of the MMED system. c) Comparison of the switching energy dissipation per decuple current gain for different types of devices. The energy consumption is 7 aJ for the 2D MoS<sub>2</sub> MMEDs (red circle). d) The leakage power for various nanometers technology nodes and typical commercial technologies to reduce power, where 2D MMEDs approach zero in design principle (red star). The abbreviation of devices is as listed: Metal-oxide-metal (MOM), metal-insulator-metal (MIM), Fin Field-Effect Transistor (FinFET), magnetic tunnel junction (MTJ), ferroelectric tunnel junction (FTJ), van der Waals heterojunction (vdWH), and Schottky barrier junction (SBJ).

technology, as the core of the ICs and the backbone of the global semiconductor industry, has developed rapidly obeying Moore's law in the past four decades and improving device performance while reducing the production cost of individual MOSFETs. Moreover, according to Dennard's law,<sup>[43]</sup> power consumption decreases as the dimensions of a device decrease; however, the short-channel effects become significant as the feature size of the semiconductor device approaches ten of nanometer. To extend the sustainable development of Moore's law, several typical commercial technologies have been implemented, such as Cu-interconnects technologies, Ge-strained channels, high- $\kappa$ /metal gates, and FinFET device structures. While the feature size approaches 7 nm, the leakage power of a single CMOS accesses the designed limit (as shown in Figure 4d and Table S5, Supporting Information). An unprecedented device architecture based on new materials and transport mechanisms should be proposed for "More than Moore" (ref. [44]) to achieve reduced power dissipation, improved integration density, and enhanced device performance. For example, our MMEDs adopt a Schottky barrier junction structure through the introduction of a strain gradient and the use of the FE to realize a large current transport modulation. Benefitting from tip-nanoindentation of the suspension structure, the static power approaches zero if mechanical losses and environmental

influence are not considered, therefore fundamentally avoiding the generation of the leakage current, which indicates the direction for the next generation of low-power devices.

### 3. Conclusion

In summary, we demonstrated a significant FE in 2D MoS<sub>2</sub> and the thickness-dependent properties of the effect, by which we fabricated high-performance MMEDs. The high electromechanical resolution/sensitivity and ultralow energy dissipation of 2D MoS<sub>2</sub> MMEDs via the FE demonstrate their potential in novel device architecture design for low power consumption ICs. The wide existence of the FE in 2D semiconductor materials provides promise for the integration of MMEDs and other functional units or devices for sensing, logic computation, human-machine interfacing, and neuromorphic devices.

### 4. Experimental Section

**Device Fabrication:** The substrate was fabricated by using UV lithography and reactive ion etching (RIE). The original substrate (10 mm × 10 mm × 1 mm) was a transparent glass with a layer of

260 nm thick ITO on top. The ITO layer was then etched to patterned array of wells with the same depth of 260 nm and various diameters (1, 2, and 3  $\mu\text{m}$ ) through 400 nm UV lithography and RIE, whose composition is HCl: HNO<sub>3</sub>: H<sub>2</sub>O = 9:1:6 (volume ratio). MoS<sub>2</sub> flakes were deposited by mechanical cleavage and exfoliation. Firstly, MoS<sub>2</sub> flakes were exfoliated from commercially available crystals of molybdenite using the scotch-tape micromechanical cleavage technique pioneered for the production of graphene. Then MoS<sub>2</sub> flakes were deposited on polymethyl methacrylate (PMMA), and the number of layers were identified by Raman spectra (HORIBA JY, FRA). Lastly, the selected MoS<sub>2</sub> flakes within three layers were deposited upon the wells in the specific location of the perforated ITO substrate by using the dry-transfer technique (Metatest, E1-M). The substrates of contact resistance device were patterned by electron beam lithography (EBL) and atomic layer deposition (ALD), and the other half was directly deposited on the adjacent ITO substrate.

**AFM Measurements:** The measurements of electrical transport properties during nanoindentation test. The electrical transport characterizations of the MoS<sub>2</sub> devices under a tip force were measured with a commercial AFM equipment Icon (Bruker, USA) with PeakForce Tuna mode. Conductive Pt/Ir-coated AFM probe (NT-MDT & TipsNano) with a radius of  $\approx 30$  nm and spring constants of  $\approx 11.8$  N m<sup>-1</sup>, and the PeakForce Tuna module with measurement ranges of 1 to 10 nA, were used to apply compressive forces and simultaneously measure the current. The PeakForce Tuna mode was used to characterize the mechanical deformation of the MoS<sub>2</sub> ultrathin film at variable mechanical loads and could precisely convert the preset voltage into applied force. The AFM probes were calibrated by a thermal tuna method, then the deflection sensitivity ( $DS$ , nm V<sup>-1</sup>) and the spring constant ( $k$ , N m<sup>-1</sup>) of the probes can be accurately gained. The precise force ( $F$ , nN) is calculated by multiplying the spring constant,  $DS$ , and Applied Voltage ( $\Delta V$ , V), which above can be formulated as  $F = k \times DS \times \Delta V$ . The gauge factor is defined as  $GF = (\Delta I/I_0)/\Delta \varepsilon$ ,  $\sigma = E\varepsilon$ , where  $I$ ,  $\varepsilon$ ,  $\sigma$ , and  $E$  represent the current, the strain, the normal pressure, and the effective Young's modulus, respectively. All the above measurements were performed in a glove box vacuum environment at room temperature.

## Supporting Information

Supporting Information is available from the Wiley Online Library or from the author.

## Acknowledgements

The authors express thanks for the support of China National Key Research and Development Plan Project from Minister of Science and Technology, China (2016YFA0202703), the National Natural Science Foundation of China (Grant Nos. 51872031, 61904013), and the University of Chinese Academy of Sciences (Grant No. E0E48909).

## Conflict of Interest

The authors declare no conflict of interest.

## Author Contributions

P.G. and M.J. contributed equally to this work. J.Z., Z.L.W., P.G., and M.J. conceived the idea. J.Z., P.G., and M.J. designed the experiments. P.G., M.J., D.G., Y.Z., L.R., and A.Y. performed the experiments and analyzed the data. P.G., M.J., D.G., W.W., A.Y., J.Z., and Z.L.W. wrote the paper. All authors discussed the results and commented on the manuscript.

## Data Availability Statement

The data that support the findings of this study are available from the corresponding author upon reasonable request.

## Keywords

2D materials, atto-joule, flexotronic effects, nano-Newton

Received: March 11, 2022

Revised: May 29, 2022

Published online:

- [1] K. L. Ekinci, M. L. Roukes, *Rev. Sci. Instrum.* **2005**, *76*, 061101.
- [2] S. L. Chen, W. J. Li, X. X. Li, W. Y. Yang, *Prog. Mater. Sci.* **2019**, *104*, 138.
- [3] Y. C. Huang, Y. Liu, C. Ma, H. C. Cheng, Q. Y. He, H. Wu, C. Wang, C. Y. Lin, Y. Huang, X. F. Duan, *Nat. Electron.* **2020**, *3*, 59.
- [4] C. S. Smith, *Phys. Rev.* **1954**, *94*, 42.
- [5] R. R. He, P. D. Yang, *Nat. Nanotechnol.* **2006**, *1*, 42.
- [6] A. A. Barlian, W. T. Park, J. R. Mallon, A. J. Rastegar, B. L. Pruitt, *Proc. IEEE* **2009**, *97*, 513.
- [7] T. Toriyama, D. Funai, S. Sugiyama, *J. Appl. Phys.* **2003**, *93*, 561.
- [8] Z. L. Wang, *Mater. Today* **2007**, *10*, 20.
- [9] Z. L. Wang, *Nano Today* **2010**, *5*, 540.
- [10] Z. L. Wang, J. H. Song, *Science* **2006**, *312*, 242.
- [11] W. Z. Wu, Z. L. Wang, *Nat. Rev. Mater.* **2016**, *1*, 16031.
- [12] C. F. Pan, J. Y. Zhai, Z. L. Wang, *Chem. Rev.* **2019**, *119*, 9303.
- [13] S. M. Kogan, *Phys. Solid State* **1964**, *5*, 2069.
- [14] A. K. Tagantsev, *Phys. Rev. B* **1986**, *34*, 5883.
- [15] G. Catalan, A. Lubk, A. H. G. Vlooswijk, E. Snoeck, C. Magen, A. Janssens, G. Rispens, G. Rijnders, D. H. A. Blank, B. Noheda, *Nat. Mater.* **2011**, *10*, 963.
- [16] H. Lu, C. W. Bark, D. E. de los Ojos, J. Alcalá, C. B. Eom, G. Catalan, A. Gruverman, *Science* **2012**, *336*, 59.
- [17] J. Narvaez, F. Vasquez-Sancho, G. Catalan, *Nature* **2016**, *538*, 219.
- [18] M. M. Yang, D. J. Kim, M. Alexe, *Science* **2018**, *360*, 904.
- [19] L. F. Wang, S. H. Liu, X. L. Feng, C. L. Zhang, L. P. Zhu, J. Y. Zhai, Y. Qin, Z. L. Wang, *Nat. Nanotechnol.* **2020**, *15*, 661.
- [20] G. Dong, S. Li, M. Yao, Z. Zhou, Y.-Q. Zhang, X. Han, Z. Luo, J. Yao, B. Peng, Z. Hu, *Science* **2019**, *366*, 475.
- [21] G. Dong, S. Li, T. Li, H. Wu, T. Nan, X. Wang, H. Liu, Y. Cheng, Y. Zhou, W. Qu, *Adv. Mater.* **2020**, *32*, 2004477.
- [22] C. Lee, X. D. Wei, J. W. Kysar, J. Hone, *Science* **2008**, *321*, 385.
- [23] M. A. Hopcroft, W. D. Nix, T. W. Kenny, *J. Microelectromech. Syst.* **2010**, *19*, 229.
- [24] P. Zubko, G. Catalan, A. Buckley, P. R. L. Welche, J. F. Scott, *Phys. Rev. Lett.* **2007**, *99*, 167601.
- [25] D. Lee, A. Yoon, S. Y. Jang, J. G. Yoon, J. S. Chung, M. Kim, J. F. Scott, T. W. Noh, *Phys. Rev. Lett.* **2011**, *107*, 057602.
- [26] R. Maranganti, P. Sharma, *Phys. Rev. B* **2009**, *80*, 054109.
- [27] T. D. Nguyen, S. Mao, Y.-W. Yeh, P. K. Purohit, M. C. McAlpine, *Adv. Mater.* **2013**, *25*, 946.
- [28] P. Zubko, G. Catalan, A. K. Tagantsev, *Annu. Rev. Mater. Res.* **2013**, *43*, 387.
- [29] G. E. Moore, *Electronics* **1965**, *38*, 114.
- [30] M. Lundstrom, *Science* **2003**, *299*, 210.
- [31] A. M. Ionescu, H. Riel, *Nature* **2011**, *479*, 329.
- [32] W. Z. Wu, Y. G. Wei, Z. L. Wang, *Adv. Mater.* **2010**, *22*, 4711.
- [33] T. Q. Trung, N. E. Lee, *Adv. Mater.* **2016**, *28*, 4338.
- [34] X. Y. Zhuang, B. He, B. Javvaji, H. S. Park, *Phys. Rev. B* **2019**, *99*, 054105.

- [35] H. L. Skriver, N. M. Rosengaard, *Phys. Rev. B* **1992**, *46*, 7157.
- [36] S. Walia, S. Balendhran, Y. C. Wang, R. Ab Kadir, A. S. Zoofakar, P. Atkin, J. Z. Ou, S. Sriram, K. Kalantar-Zadeh, M. Bhaskaran, *Appl. Phys. Lett.* **2013**, *103*, 232105.
- [37] H. J. Conley, B. Wang, J. I. Ziegler, R. F. Haglund, S. T. Pantelides, K. I. Bolotin, *Nano Lett.* **2013**, *13*, 3626.
- [38] W. Z. Wu, L. Wang, Y. L. Li, F. Zhang, L. Lin, S. M. Niu, D. Chenet, X. Zhang, Y. F. Hao, T. F. Heinz, J. Hone, Z. L. Wang, *Nature* **2014**, *514*, 470.
- [39] C. J. Brennan, R. Ghosh, K. Koul, S. K. Banerjee, N. S. Lu, E. T. Yu, *Nano Lett.* **2017**, *17*, 5464.
- [40] L. L. Shu, S. M. Ke, L. F. Fei, W. B. Huang, Z. G. Wang, J. H. Gong, X. N. Jiang, L. Wang, F. Li, S. J. Lei, Z. G. Rao, Y. B. Zhou, R. K. Zheng, X. Yao, Y. Wang, M. Stengel, G. Catalan, *Nat. Mater.* **2020**, *19*, 605.
- [41] J. Jiang, Z. Z. Chen, Y. Hu, Y. Xiang, L. F. Zhang, Y. P. Wang, G. C. Wang, J. Shi, *Nat. Nanotechnol.* **2021**, *16*, 894.
- [42] J. S. Bunch, A. M. van der Zande, S. S. Verbridge, I. W. Frank, D. M. Tanenbaum, J. M. Parpia, H. G. Craighead, P. L. McEuen, *Science* **2007**, *315*, 490.
- [43] R. H. Dennard, F. H. Gaensslen, H. N. Yu, V. L. Rideout, E. Bassous, A. R. Leblanc, *IEEE J. Solid-State Circuits* **1974**, *SC 9*, 256.
- [44] M. M. Waldrop, *Nature* **2016**, *530*, 144.